Title

Multi-layer nanoarrays sandwiched by anodized aluminium oxide membranes: an approach to an inexpensive, reproducible, highly sensitive SERS substrate

Journal

Nanoscale, 10(34)

ISSN

2040-3364

Authors

Zhao, Chengchun
Zhu, Yuan
Chen, Li
et al.

Publication Date

2018-08-30

DOI

10.1039/c8nr05875j

Peer reviewed

Nanoscale

PAPER

View Article Online
View Journal | View Issue

Cite this: *Nanoscale*, 2018, **10**, 16278

Multi-layer nanoarrays sandwiched by anodized aluminium oxide membranes: an approach to an inexpensive, reproducible, highly sensitive SERS substrate†

Chengchun Zhao, [a] Yuan Zhu,*[a,b] Li Chen,*[b] Shaoxin Zhou,[a] Yuquan Su,[c] Xu Ji,[c] Anqi Chen,[a] Xuchun Gui, [c] Zikang Tang[d] and Zhaowei Liu[c]

A large-scale sub-5 nm nanofabrication technique is developed based on double layer anodized aluminium oxide (AAO) porous membrane masking. This technique also provides a facile route to form multilayer nano-arrays (metal nanoarrays sandwiched by AAO membranes), which is very challenging for other techniques. Normally the AAO mask has to be sacrificed, yet in this work it is preserved as a part of the nanostructure. The preserved AAO layers as the support for the second/third layer of the metal arrays provide a high-refractive index background for the multilayer metal arrays. This background concentrates the local E-field more significantly and results in a much higher Surface-Enhanced Raman Spectroscopy (SERS) signal than single layer metal arrays. This technique may lead to the advent of an inexpensive, reproducible, highly sensitive SERS substrate. Moreover, the physical essence of the plasmonic enhancement is unveiled by finite element method based numerical simulations. Enhancements from the gaps and the multilayer nanostructure agree very well with the experiments. The calculated layer-by-layer electric field distribution determines the contribution from different layers and provides more insights into the 3D textured structure.

Received 20th July 2018,
Accepted 1st August 2018

DOI: 10.1039/c8nr05875j

rsc.li/nanoscale

Introduction

Large-scale arrays of nanostructures on substrates are used in many fields such as data storage, nano-optics, and biosensing. To fabricate these nano-arrays, lithographic methods like E-beam lithography (EBL), focused ion beam (FIB), and nano-imprinting are commonly used.[1–6] A common shortcoming of the above techniques is that the facilities needed are complex and expensive, and the implementation steps required are tedious. Especially for large-scale sub-5 nm gap fabrication, which is very crucial for the application of gap plasmons,[7–15] none of the above techniques provides a satisfactory solution.

As an alternative, the method based on ultrathin anodized aluminium oxide (AAO) templates is widely investigated because it is cost effective, scalable and compatible with different synthesis techniques.[16–24] So far, however, the smallest gap size from single layer (SL) AAO membrane masking is around 10–15 nm because it is determined by the AAO pore wall size and the thinnest wall size is ~10 nm. In this work, for the first time, we stacked two ultrathin AAO membranes and used this double-layer (DL) membrane as an evaporation mask. After deposition, the average gap size is ~4 nm and the smallest one is even close to ~1 nm.

More importantly, this double layer masking provides a facile route to form multilayer nano-arrays (metal nanoarrays sandwiched between AAO membranes), which is very challenging and tedious for lithography-based methods.

Here we present large-scale layered Ag arrays with sub-5 nm gaps. Both the ultra-small gaps and the multilayer nanostructures are found to be very constructive for local electric field (E_{loc}) enhancement. This enhancement is observed by Surface-Enhanced Raman Spectroscopy (SERS) tests. And its physical essence is unveiled by theoretical calculations. The calculated enhancements from the gaps and the multilayer

[a]*College of Innovation and Entrepreneurship, Southern University of Science and technology, Shenzhen 518055, China. E-mail: zhuy3@sustc.edu.cn*
[b]*Department of Electrical and Computer Engineering, University of California, San Diego, La Jolla, California 92093, USA. E-mail: yili.fchen@gmail.com*
[c]*State Key Lab of Optoelectronic Materials and Technologies, School of Electronics and Information Technology, Sun Yat-sen University, Guangzhou, 510275, P. R. China*
[d]*The Institute of Applied Physics and Materials Engineering, University of Macau, Avenida da Universidade, Taipa, Macau, China*

†Electronic supplementary information (ESI) available: Outline of the fabrication processes, some more patterns, low-magnification SEM image of AAO membranes and Ag nanoparticle arrays, comparison of Raman spectra, concentration-dependent SERS spectra, EF calculation details, single-layer AAO mask for comparison, and the 3D model for simulations. See DOI: 10.1039/c8nr05875j

nanostructure well reproduced the experimental results. More insights into the sandwich structure are given through the layer-by-layer analysis of the E-field distribution. In addition, this approach provides a low-cost platform for the preparation of an ordered multi-layer nanostructure on large substrates since there is no need for lithographic processes and clean-room facilities.

Results and discussion

One purpose of using two overlaid AAO membranes is to acquire unlimited mask pattern variations for nanofabrication. Fig. 1 demonstrates the concept and some typical patterns it can achieve. The pore structure of each layer (Fig. 1a) and their overlaid offset/angle determine the mask patterns (Fig. 1b–d). The corresponding SEM images of mask structures (Fig. 1e–g) and deposited Ag arrays (Fig. 1h–j) agree perfectly well with our expectations as shown in Fig. 1b–d. By this method, dimer arrays (Fig. 1h), trimer arrays (Fig. 1i) and sunflower configurations (Fig. 1j) are easy to acquire. Some more patterns are illustrated in the ESI (Fig. S1†). In theory, operations such as translational shifting or rotating one layer relative to the other could produce an unlimited variety of patterns. The pattern category can be further expanded by tuning the pore shape, pore size and array pattern. The use of overlaid AAO membranes provides a general route to fabricate complex metal nanoparticle arrays on a large scale, *e.g.* in cm-level (Fig. S3e†). Although the long-range pattern periodicity is yet to be improved, high-density sub-5 nm gaps and multilayer nanostructures can be achieved with high reliability and reproducibility. For single layer AAO, the ordered range is 1–5 μm for each domain (Fig. S4†). For double layer AAO, the ordered range for each domain decreases to 0.5–1.5 μm (see Fig. S5a–c†). These pattern rules are passed down to the resulting Ag nanoparticle arrays (see Fig. S5d–f†). The other two purposes of double-layer AAO masking are to realize high-density sub-5 nm gaps and multilayer nanostructures.

Theoretically, for SL masking, the gap size should not be less than the wall thickness (at least 10 nm to be transferable) due to the shadowing effect (Fig. S9i & S9j†). DL masking should overcome this limit. First the support of the bottom layer membrane allows the use of thinner-wall upper layer AAO. Second the suspension of the upper layer facilitates the off-normal/angled deposition. During deposition (Fig. 2a), the metal gas flow bypasses the bottom edges of the suspended

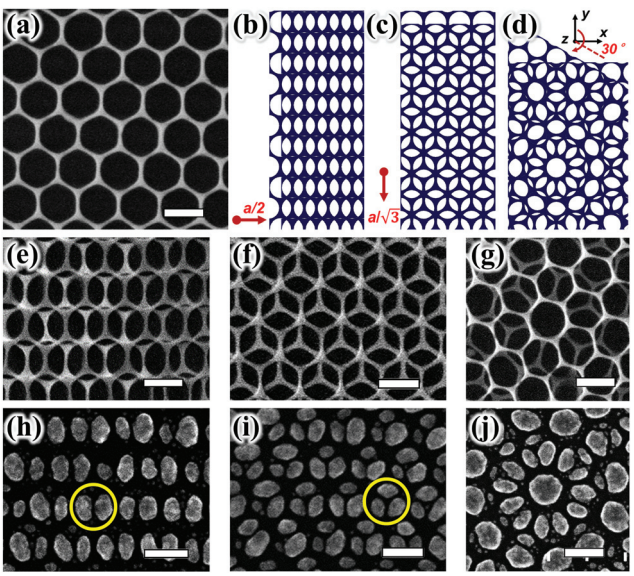

Fig. 1 (a) High-magnification top-view SEM image of the AAO membrane used in this work. (b–d) Three typical schematic patterning formed by two stacked AAO membranes. Relative to the bottom membrane layer, upper layer (b) shifts $a/2$ left; (c) shifts $a/\sqrt{3}$ down; (d) rotates 30° clockwise. Here a is the distance of two neighboring pore centers. (e–f) SEM images of double AAO membranes corresponding to (b–d), respectively. (h–j) Ag nanoparticle arrays fabricated by double AAO membrane masking, corresponding to (b–d). Ag nanostructures in the yellow circles are "dimer" and "trimer", respectively. Scale bars: 100 nm.

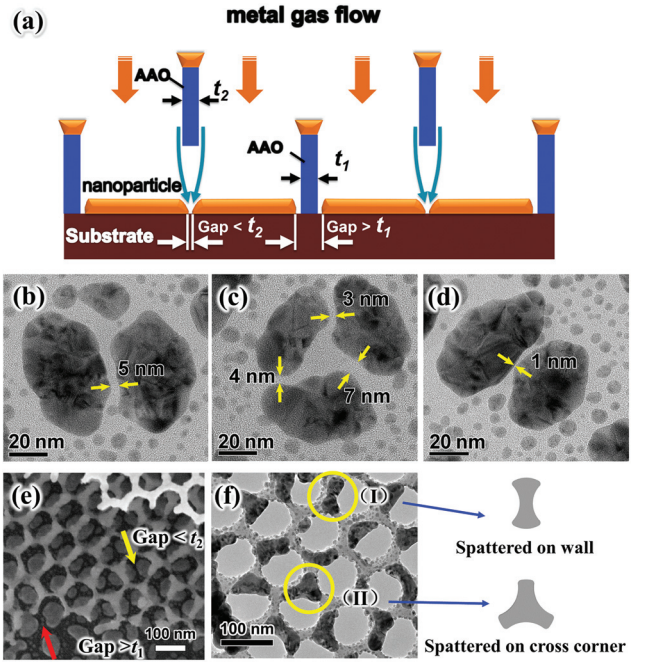

Fig. 2 (a) Schematic illustration of the formation mechanism of the ultra-small gaps. Normally DL masking results in two categories of gap size: Gap > t_1 and Gap < t_2. Here t_1 and t_2 stand for lower and upper layer wall thickness, respectively. Both t_1 and t_2 are ~10 nm according to statistics shown in Fig. S9.† During deposition, the angled metal gas flow bypasses the bottom edges of the suspended pore walls and arrives at the surface of the substrate right under the walls (curved arrows). The off-normal arrivals of metal atoms render gaps smaller than the wall thickness. (b–d) High magnification TEM images of Ag dimer and trimer by DL masking, showing the sub-5 nm gaps. (e) SEM image of Ag arrays from DL AAO masking with part of AAO remaining. As indicated by the arrows, the small gap size is from the upper layer masking (Gap < t_2) while the large gap size is from the bottom layer masking (Gap > t_1). (f) TEM image of the bottom layer of the stacked AAO membranes (t_{Ag} = 25 nm), and two typical Ag nanostructures are shown.

pore walls and arrives at the surface of the substrate right under the walls (curved arrows in Fig. 2a). The off-normal arrivals of metal atoms fill the space under the suspended upper layer wall and result in gaps smaller than the wall thickness (Fig. 2b–d).

Compared to many studies on SL AAO membrane-based nanofabrication,[17–24] our pioneering use of double layer AAO membranes (DL AAO) faces a new challenge in the membrane transfer and overlay process. Here we employ a new method to overcome it (Fig. S2†). Briefly, SL AAOs are flatly attached onto the polymethyl methacrylate (PMMA) support. A thin acetone film is sprayed on the substrate followed by the attachment of two layers of the PMMA/AAO film. The acetone layer prevents the formation of air bubbles between the PMMA/AAO and substrate. After acetone evaporation, a part of the PMMA film is dissolved and the remaining part is firmly adhered to the substrate. The substrate is then heated at a temperature a little higher than the glass transition temperature of PMMA in order to allow the wavy and rough PMMA/AAO film to make full and flat contact with the target substrate. PMMA can be removed by thermal decomposition. The thermal decomposition of PMMA is not affected by the atmosphere (such as nitrogen, argon or vacuum), and the predominant product is monomer MMA (>90%). Besides this, products such as CO, CO_2, OH, and CH_4 are formed simultaneously.[25] All of our fabrication procedures are carried out in a routine laboratory rather than a clean room. The detailed processes are described in the Experimental section and ESI.†

In order to evaluate the performance of the prepared layered Ag arrays, SERS experiments on different layer-structures were carefully conducted and the results are shown in Fig. 3. The inset of Fig. 3 depicts the detailed structure of five different samples. The major differences are: first, whether the single layer (SL) or double layer (DL) masking is used, and then, how many (0, 1 or 2) layers of masking membranes were left intentionally after deposition. The SERS spectra of all five possible combinations are arranged as curve (1)–(5). Here 4-aminothiophenol (4-ATP) is used as the model Raman probe. Four b2 modes (1581, 1442, 1395, and 1147 cm^{-1}) and two a1 modes (1081 and 1194 cm^{-1}) are observed in the resulting spectra.[26] Here the Ag deposition thickness is 25 nm. The spectra of other Ag deposition thicknesses (15 nm and 35 nm) are shown in Fig. S7.†

We calculated the enhancement factor (EF) of each sample based on the 1081 cm^{-1} peak and summarized them in Table 1. By comparing the samples with AAO and without AAO separately, we noticed that the EF of nanostructures from DL AAO is generally 2–4 times larger than that of nanostructures from SL AAO. This is because DL masking has two advantages over SL masking. First, the DL AAO masking provides more chances to obtain rice-like shaped particles rather than the uniform half-balls or circular truncated cones (Fig. S9†) by SL AAO masking.[16] Fig. 2b–d presents the TEM images of two basic nanostructures formed by DL AAO masking: dimer and trimer. The Ag nanoparticles in both dimer and trimer are rice-shaped and have sharp tips (Fig. 1h & i). Well-defined

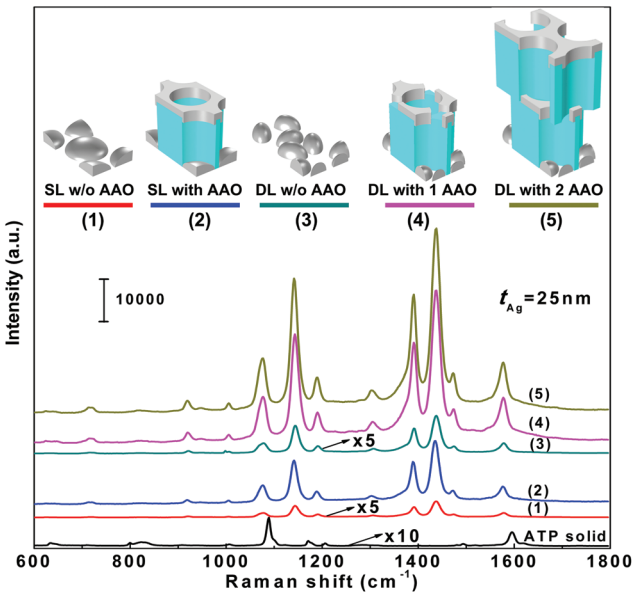

Fig. 3 SERS spectra of different layer-structures: (1) Ag nanostructures fabricated by single layer AAO masking with no AAO membrane left (SL w/o AAO, red line); (2) Ag nanostructures fabricated by single layer AAO masking with the AAO membrane remaining in position (SL with AAO, blue line); (3) Ag nanostructures fabricated by double layer AAO masking with no AAO membrane left (DL w/o AAO, dark cyan line); (4) Ag nanostructures fabricated by double layer AAO masking with only the bottom layer AAO membrane left (DL with 1 AAO, magenta line); (5) Ag nanostructures fabricated by double layer AAO masking with the both AAO membranes remaining in position (DL with 2 AAO, dark yellow line). 4-Aminothiophenol (4-ATP) is used as the model Raman probe, and the excitation laser wavelength is 514 nm. The bottom black line is the spectrum of solid 4-ATP. All the other samples were soaked in 4-ATP solution (10^{-3} M) for 30 min, and rinsed several times with ethanol and gently dried with N_2 stream, which ensured the formation of only a monolayer of 4-ATP over the surface of the nanoparticles. Here the Ag deposition thickness is 25 nm. Insets: Schematic diagram of different layer-structures.

Table 1 Enhancement factor of different layer-structures at 1081 cm^{-1} (calculation details see Table S1)

	Enhancement factor				
t_{Ag} (nm)	SL w/o AAO	SL with AAO	DL w/o AAO	DL with 1 AAO	DL with 2 AAO
15	9.67×10^2	1.08×10^4	1.59×10^3	3.55×10^4	3.18×10^4
25	1.06×10^3	1.52×10^4	3.28×10^3	5.46×10^4	4.41×10^4
35	1.09×10^3	1.69×10^4	3.64×10^3	6.56×10^4	2.80×10^4

edges, corners or tips could enhance E_{loc} and thus the Raman signal.[27–30] Second, DL AAO masking combined with angled deposition produces a large density of ultra-small gaps (1–7 nm, Fig. 2b–d). The gap plasmons enhance E_{loc} at the rate of R^{-3}, where R is the gap size.[31]

To reveal the gap-mask relationship, we intentionally left part of DL mask after deposition and observed it with a SEM. Fig. 2e clearly shows that the ultra-small gaps are from the

upper layer masking (yellow arrow) rather than the lower layer masking (red arrow). The angled deposition by wedging the sample at a certain angle could further narrow the gap. But the angle should be very carefully tuned because over-angled wedging could cause the particles to merge thus diminishing the gap.

The significant enhancement from the remaining AAO is also revealed in Fig. 3 and Table 1. This enhancement, 10–20 times larger, is hypothesized to be generated from the ultra-narrow corner between the outer surface of the Ag particle and the AAO wall. The AAO pore walls, with a high refractive index, increased the localization of electric field in the vicinity of metal surfaces quite near to the pore walls and finally result in a higher electric field intensity. Compared to DL with 1 AAO, the enhancement in DL with 2 AAO is slightly lower, implying that the top-layer AAO and the Ag layer on it may not contribute to the Raman signal.

We also performed concentration dependent SERS for 4-ATP on Ag nanostructures fabricated by double AAO membranes with an Ag deposition thickness of 25 nm and the AAO remaining (Fig. S8†). The detection limit of the substrate can be roughly estimated to be 10^{-9} M which is among the best compared with other Ag nanostructures reported in the literature as shown in Table S2.†

The underlying physical essence of above enhancements has been further investigated through a full wave numerical simulation with commercial software COMSOL Multiphysics. The model and calculation details can be found in the Experimental section and ESI (Fig. S10–13†). Fig. 4 summarises some important results. In order to simplify the simulation, we choose two typical configurations that appeared in the DL AAO masking obtained patterns: dimer (Fig. 1h and Type A in Fig. 4) and trimer (Fig. 1i and Type B in Fig. 4), and compare their enhancement effect with a uniform circular particle array from SL AAO masking. The gap sizes for dimer and trimer are 4 nm in the simulation referring to the experimental average value as measured in Fig. 2b–d. Since the Raman signal is proportional to $(|E_{loc}|^4/|E_0|^4)$, the relative field enhancement of each structure is presented in the form of $(\lg(|E_{loc}|^4/|E_0|^4))$, where E_0 is the amplitude of the input E-field, and the logarithm scale is taken to show the order of enhancement factor with better contrast (Fig. 4).

From panels a1, b1 and c1 in Fig. 4, the dimer array (with 4 nm gap) contributes a 1.5 order of magnitude enhancement over the uniform circular particle array. And the trimer array (with the same 4 nm gap) presents even a 1.2 orders of magnitude enhancement over the dimer array. Theoretically, the sharpening of the particle tips/edges and the narrowing of the gap size both contribute to E-field enhancement. In Fig. 4, the tips of rice-shaped monomers and the gaps between them concentrate the electric field enhancement, known as "hot spots". For the dimer array, the long axes are parallel, *i.e.* the gaps and tips are spatially isolated from each other so that they contribute to the E-field enhancement separately (maximum $\lg(|E_{loc}|^4/|E_0|^4) \sim 7.5$, see Fig. 4b1). For the trimer array, the three monomers are in circular head-to-tail style, which

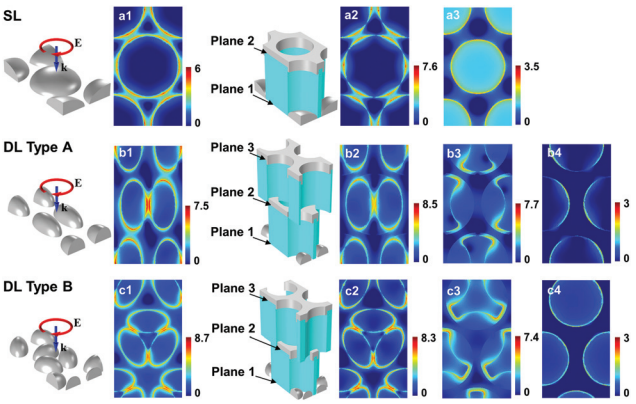

Fig. 4 Electric field distribution $(\lg(|E|^4/|E_0|^4))$ on different planes of Ag nanostructures based on (a1–a3) SL AAO (SL) and two typical patterns of DL AAO: (b1–b4) Type A and (c1–c4) Type B. (a1, b1, and c1) refer to Ag nanoparticle arrays without AAO membranes, while others refer to Ag nanostructures with remaining AAO. Plane 1 is the surface of the substrate. Plane 2 and plane 3 are the upper surface of the bottom AAO and top AAO, respectively. (a2, b2, and c2), (a3, b3, and c3), and (b4 and c4) correspond to plane 1, plane 2, and plane 3, respectively. The interpore distance, pore diameter, and height of the AAO membrane are 100 nm, 90 nm, and 120 nm, respectively. The deposition thickness of Ag is 25 nm. The geometries of the models were derived from the TEM images of Ag nanoparticles and the detailed parameters can be found in the ESI.† The colour bars demonstrate the order of enhancement factor.

induces an additional tip-gap coupling effect and thus produces an even higher E-field enhancement (maximum $\lg(|E_{loc}|^4/|E_0|^4) \sim 8.7$, see Fig. 4c1).

Panels a2–a3, b2–b4 and c2–c4 in Fig. 4 demonstrate the layer-by-layer analysis of E-field distribution. The E-field enhancement in Ag nanoparticle arrays with the AAO membrane remaining (Fig. 4a2 and b2) is higher than those with the AAO membrane removed (Fig. 4a1 and b1). Due to the existence of the AAO membrane, ultra-narrow corners are formed between the outer surface of Ag particles and the nearby AAO wall (Fig. S14†). Stronger light confinement is achieved due to the increased refractive index around the Ag particles (the refractive index of AAO is 1.76). And thus we can get even higher E_{loc} in these ultra-narrow corners. Fig. 4a2 and b2 show that the further enhancement is mainly distributed on the outer surface of the Ag nanoparticle, other than the inner gaps. In the case of the trimer (Fig. 4c2), this is also true but less obvious due to the strong coupling between the head to head particles. The coupling between the Ag nanoparticle and AAO wall relatively reduces the coupling within Ag nanoparticles so that the maximum E-field in Fig. 4c2 is slightly lower but with a larger enhanced area compared to Fig. 4c1.

Moreover, the extra support of the remaining AAO membranes makes it possible to have second/third layers of Ag nanostructures (*e.g.* Plane 2 and Plane 3 in Fig. 4). The calculations show that the Ag nanostructures on Plane 2 sandwiched between two AAO membranes as shown in Fig. 4b3 and c3 (see TEM images in Fig. 2f) can also provide a large

contribution to the enhancement. The top layer Ag nanostructures are much less influential. This agrees well with our early observation from Table 1: the enhancement factor from DL with 2 AAO is close to or even slightly lower than that from DL with 1 AAO.

Experimental

Fabrication of AAO

The ultrathin AAO membranes are obtained from Topmembranes Technology Co., Ltd. The fabrication method they use is as follows: high-purity (99.999%) Al foils are degreased with acetone and electrochemically polished. The foil then is anodized in oxalic acid solution (0.3 M) at 40 V. The anodic oxide layer is removed in a mixture of H_3PO_4 and H_2CrO_4. The specimen is anodized again for a short time. Subsequently, the pores were enlarged in aqueous H_3PO_4 solution (5 wt%) at 30 °C.

Transfer of AAO

A PMMA layer was coated on top of the alumina layer. After that, the Al layer was removed in a mixture of $CuSO_4$ and HCl solution. The removal of the thin barrier layer was carried out in H_3PO_4 solution (5 wt%) at 30 °C. The silicon wafer and fused silica were taken as substrates. Acetone was dropwise added onto substrates to form a thin acetone layer. Then, one or two stacked PMMA/AAO sheets were gently applied to the substrate. After drying, the sample was heated at 180 °C in air for 20 min. PMMA was removed *via* annealing the sample at 400 °C under flowing N_2 for 10 min in a rapid thermal processing system.

Metal deposition and lift-off

Pure Ag (99.99%) films of various thicknesses were deposited over the AAO masks using electron-beam evaporation at a rate of 0.1 nm s^{-1}. The working pressure during the evaporation was $<8 \times 10^{-6}$ Torr. The temperature of the sample chamber was kept at 25 °C during the entire evaporation process. The thickness of the Ag film was measured by using a quartz crystal microbalance. After the deposition, the membrane was removed using Kapton tape, leaving Ag nanoparticle arrays on the substrate.

Characterization

The morphology of the samples was studied using a scanning electron microscope (SEM) Hitachi S-4800. Transmission electron microscopy (TEM) images were obtained using a FEI Tecnai G2 F30 (200 kV) transmission electron microscope.

SERS

To prepare the substrate for SERS, the samples corresponding to curves (1)–(5) in Fig. 3a and Fig. S7a–e† were soaked in an ethanol solution (10^{-3} M) of 4-ATP for 30 min. After soaking, the samples were rinsed several times with ethanol and gently dried with N_2 stream. The rinsing process ensured the formation of only a monolayer of 4-ATP over the surface of the nanoparticles. Raman spectra were recorded by using a confocal microprobe Raman spectrometer (JY, LABRAM-HR, France) with a 514 nm argon ion laser (1.2 mW). The excitation light for Raman spectra is un-polarized.

Numerical simulations

In order to examine the near field enhancement of the Ag nanoparticle arrays, full-wave numerical simulations were performed by using finite-element method based commercial software, COMSOL Multiphysics (V5.2a). The model was created in a three-dimensional space and two ports were respectively positioned at opposite sides working as the input and output. The circular polarized plane waves were incident normally onto one unit cell of the Ag nanoparticles array, where the periodic boundary condition was set to describe the whole structure. The parameters of geometries are established based on the TEM images and deposition process. The refractive indices of Ag and Al_2O_3 were taken from those reported by Babar *et al.* and Malitson *et al.*,[32,33] respectively. The refractive index of the quartz substrate was set to be $n = 1.5$.

Conclusions

We have developed a new sub-5 nm nanofabrication technique based on double layer AAO membranes masking, which can be performed on a large-scale, and is cost-effective and cleanroom free. The ordinary single layer AAO masking could only fabricate ~15 nm gaps due to the shadowing effect (Fig. S9†). We avoid this limitation by using two overlaid layers of AAO membranes. First the support of the bottom layer membrane allows the use of thinner-wall upper layer AAO and second the suspension of the upper layer facilitates the off-normal/angled deposition. The off-normal arrivals of metal atoms fill part of the space under the upper layer and the angled deposition could narrow the gap further.

More importantly, this double layer masking technique provides a facile route to form multilayer nano-arrays (metal nanoarrays sandwiched between AAO membranes), which is very challenging for other techniques. This multilayer nanostructure is found to be very constructive for local E-field (E_{loc}) enhancement. The SERS EF grows by an additional 3× or 4×. This technique may lead to the advent of inexpensive, reproducible, highly sensitive SERS substrates.

The physical essence of the plasmonic enhancement is unveiled by numerical simulation. Enhancements from the gaps and the multilayer nanostructure agree very well with the experiments. The gap-tip coupling effect and the Ag–AAO coupling effect are revealed by 3D analysis of the E_{loc} distribution. The remaining AAO layers provide the support for the second/third layer of metal arrays and at the same time, provide a high-refractive index background for multilayer metal arrays. This background with a strong light confinement ability concentrates E_{loc} more significantly and results in a much higher SERS signal.

Conflicts of interest

There are no conflicts to declare.

Acknowledgements

The authors gratefully acknowledge financial support from Shenzhen Peacock Program technology innovation 20170725111023935 and the National Science Foundation for Young Scientists of China (Grant No. 51702277). Dr C. Zhao thanks Dr Y. Shen and S. J. Lin for their discussions. C. C. Zhao and Y. Zhu contributed equally to this work.

Notes and references

1 H. G. Duan, H. L. Hu, K. Kumar, Z. X. Shen and J. K. W. Yang, *ACS Nano*, 2011, **5**, 7593.
2 V. R. Manfrinato, A. Stein, L. H. Zhang, C. Y. Nam, K. G. Yager, E. A. Stach and C. T. Black, *Nano Lett.*, 2017, **17**, 4562.
3 A. N. Abbas, G. Liu, L. Liu, L. Y. Zhang, H. Liu, D. Ohlberg, W. Wu and C. W. Zhou, *ACS Nano*, 2014, **8**, 1538.
4 F. Santoro, W. T. Zhao, L. Joubert, L. T. Duan, J. Schnitker, Y. van de. Burgt, H. Y. Lou, B. F. Liu, A. Salleo, L. F. Cui, Y. Cui and B. X. Cui, *ACS Nano*, 2017, **11**, 8320.
5 H. Lee and G. Y. Jung, *Microelectron. Eng.*, 2005, **77**, 42.
6 K. Hasna, A. Antony, J. Puigdollers, K. R. Kumar and M. K. Jayaraj, *Nano Res.*, 2016, **9**, 3075.
7 H. H. Wang, C. Y. Liu, S. B. Wu, N. W. Liu, C. Y. Peng, T. H. Chan, C. F. Hsu, J. K. Wang and Y. L. Wang, *Adv. Mater.*, 2006, **18**, 491.
8 J. Theiss, P. Pavaskar, P. M. Echternach, R. E. Muller and S. B. Cronin, *Nano Lett.*, 2010, **10**, 2749.
9 W. Q. Zhu, M. G. Banaee, D. X. Wang, Y. Z. Chu and K. B. Crozier, *Small*, 2011, **7**, 1761.
10 V. Merk, J. Kneipp and K. Leosson, *Adv. Opt. Mater.*, 2013, **1**, 313.
11 X. S. Chen, H. R. Park, M. Pelton, X. J. Piao, N. C. Lindquist, H. Im, Y. J. Kim, J. S. Ahn, K. J. Ahn, N. Park, D. S. Kim and S. H. Oh, *Nat. Commun.*, 2013, **4**, 2361.
12 J. W. Qi, Y. X. Xiang, W. G. Yan, M. Li, L. S. Y. Yang, Z. Q. Chen, W. Cai, J. Chen, Y. D. Li, Q. Wu, X. Y. Yu, Q. Sun and J. Xu, *J. Phys. Chem. C*, 2016, **120**, 24932.
13 J. M. Nam, J. W. Oh, H. Lee and Y. D. Suh, *Acc. Chem. Res.*, 2016, **49**, 2746.
14 W. J. Liu, Y. Shen, G. H. Xiao, X. Y. She, J. F. Wang and C. J. Jin, *Nanotechnology*, 2017, **28**, 075301.
15 D. G. Baranov, M. Wersäll, J. Cuadra, T. J. Antosiewicz and T. Shegai, *ACS Photonics*, 2018, **5**, 24.
16 Y. Lei and W. K. Chim, *Chem. Mater.*, 2005, **17**, 580.
17 W. Lee, H. Han, A. Lotnyk, M. A. Schubert, S. Senz, M. Alexe, D. Hesse, S. Baik and U. Gösele, *Nat. Nanotechnol.*, 2008, **3**, 402.
18 Y. Lei and W. K. Chim, *J. Am. Chem. Soc.*, 2005, **127**, 1487.
19 Z. B. Zhan, F. Grote, Z. J. Wang, R. Xu and Y. Lei, *Adv. Energy Mater.*, 2015, **5**, 1501654.
20 G. Tian, F. Y. Zhang, J. X. Yao, H. Fan, P. L. Li, Z. W. Li, X. Song, X. Y. Zhang, M. H. Qin, M. Zeng, Z. Zhang, J. J. Yao, X. S. Gao and J. M. Liu, *ACS Nano*, 2016, **10**, 1025.
21 M. H. Wu, L. Y. Wen, Y. Lei, S. Ostendorp, K. Chen and G. Wilde, *Small*, 2010, **6**, 695.
22 A. Al-Haddad, Z. B. Zhan, C. L. Wang, S. Tarish, R. Vellacheria and Y. Lei, *ACS Nano*, 2015, **9**, 8584.
23 C. C. Zhao, Y. Zhu, Y. Q. Su, Z. Y. Guan, A. Q. Chen, X. Ji, X. C. Gui, R. Xiang and Z. K. Tang, *Adv. Opt. Mater.*, 2015, **3**, 248.
24 Z. P. Huang, X. X. Zhang, M. Reiche, L. F. Liu, W. Lee, T. Shimizu, S. Senz and U. Gösele, *Nano Lett.*, 2008, **8**, 3046.
25 W. R. Zeng, S. F. Li and W. K. Chow, *J. Fire Sci.*, 2002, **20**, 297.
26 S. J. Guo, S. J. Dong and E. K. Wang, *Cryst. Growth Des.*, 2009, **9**, 372.
27 W. X. Sun and Z. X. Shen, *J. Opt. Soc. Am. A*, 2003, **20**, 2254.
28 J. Grand, M. L. de la. Chapelle, J.-L. Bijeon, P.-M. Adam, A. Vial and P. Royer, *Phys. Rev. B: Condens. Matter Mater. Phys.*, 2005, **72**, 033407.
29 J. M. McLellan, Z. Y. Li, A. R. Siekkinen and Y. N. Xia, *Nano Lett.*, 2007, **7**, 1013.
30 Y. Yang, S. Matsubara, L. M. Xiong, T. Hayakawa and M. Nogami, *J. Phys. Chem. C*, 2007, **111**, 9095.
31 E. C. Le Ru, E. Blackie, M. Meyer and P. G. Etchegoin, *J. Phys. Chem. C*, 2007, **111**, 13794.
32 S. Babar and J. H. Weaver, *Appl. Opt.*, 2015, **54**, 477.
33 I. H. Malitson and M. J. Dodge, *J. Opt. Soc. Am.*, 1972, **62**, 1405.